

# Physical Conditions in the X-ray Emission-line Gas in NGC 1068

S. B. Kraemer <sup>1</sup>, N. Sharma <sup>2</sup>, T. J. Turner <sup>2</sup>, Ian M. George <sup>2</sup>

and

D. Michael Crenshaw <sup>3</sup>

## ABSTRACT

We present a detailed, photoionization modeling analysis of *XMM-Newton*/Reflection Grating Spectrometer observations of the Seyfert 2 galaxy NGC 1068. The spectrum, previously analyzed by Kinkhabwala et al. (2002), reveals a myriad of soft-X-ray emission lines, including those from H- and He-like carbon, nitrogen, oxygen, and neon, and M- and L-shell iron. As noted in the earlier analysis, based on the narrowness of the radiative recombination continua, the electron temperatures in the emission-line gas are consistent with photoionization, rather than collisional ionization. The strengths of the carbon and nitrogen emission lines, relative to those of oxygen, suggest unusual elemental abundances, which we attribute to star-formation history of the host galaxy. Overall, the emission-lines are blue-shifted with respect to systemic, with radial velocities  $\sim 160 \text{ km s}^{-1}$ , similar to that of [O III]  $\lambda 5007$ , and thus consistent with the kinematics and orientation of the optical emission-line gas and, hence, likely part of an AGN-driven outflow. We were able to achieve an acceptable fit to most of the strong emission-lines with a two-component photoionization model, generated with Cloudy. The two components have ionization parameters and column densities of  $\log U = -0.05$  and  $1.23$ , and  $\log N_{\text{H}} = 20.85$  and  $21.2$ , and covering factors of  $0.35$  and  $0.84$ , respectively. The total mass of the X-ray gas is roughly of an order of magnitude greater than the mass of ionized gas determined from optical and near-IR spectroscopy, which indicates that it may be the dominant component of the narrow line region. Furthermore, we suggest that the medium which produces the scattered/polarized optical emission in NGC 1068 possesses similar physical characteristics to those of the more highly-ionized of the X-ray model components.

---

<sup>1</sup>Institute for Astrophysics and Computational Sciences, Department of Physics, The Catholic University of America, Washington, DC 20064

<sup>2</sup>Department of Physics, University of Maryland Baltimore County, Baltimore, MD 21250, U.S.A

<sup>3</sup>Department of Physics and Astronomy, Georgia State University, Astronomy Offices, One Park Place South SE, Suite 700, Atlanta, GA 30303

*Subject headings:* galaxies: active - galaxies: individual: NGC 1068 - galaxies: Seyfert - X-rays: galaxies

## 1. Introduction

Active Galactic Nuclei (AGN) of which Seyfert galaxies are relatively low luminosity ( $L_{bol} \lesssim \text{several} \times 10^{45} \text{ ergs s}^{-1}$ ) examples in the local Universe ( $z \lesssim 0.1$ ), are thought to be powered by accretion of matter onto super-massive black holes, which reside at the gravitational centers of the host galaxies. The properties of Seyfert galaxies and how these are understood within the context of the unified model (Antonucci 1993) have been discussed in several of our previous papers (e.g., Kraemer et al. 2009). However, it is useful in the context of this paper to mention the scales of the various regions that contribute to the spectra of Seyferts. The continuum source, which is  $\sim$  light hours in extent (e.g., Edelson et al. 1996) and surrounding broad emission-line region, which ranges in size from several to tens of light days (e.g., Peterson et al. 2004), are only directly observable in Seyfert 1 galaxies. In contrast, the narrow-line region (NLR), which is comprised of lower-density gas in which the forbidden lines and narrower components of the permitted lines form, can extend out to  $\sim 1$  kpc (e.g., Pogge 1988).

Due to its proximity, the Seyfert 2 nucleus of the barred-spiral galaxy NGC 1068 (Bland-Hawthorn et al. 1997) is the most extensively studied such object to date. Redshift-independent distance estimates place the host galaxy between 10 and 16 Mpc away (e.g. Tully et al. 2009; Sofue 1991). To be consistent with the bulk of the current literature here we adopt the mean value of 12.65 Mpc from NED<sup>1</sup>, such that 1'' is roughly equivalent to 60 pc.

Ground-based narrowband images of the NLR in NGC 1068 show that the optical emission-line gas possesses a biconical morphology, roughly parallel to the major axis of the radio emission, extended northeast and southwest of the nucleus (Pogge 1988). Narrow-band optical images obtained with the *Hubble Space Telescope (HST)* revealed that the inner NLR also possesses a biconical morphology (e.g., Evans et al. 1991) and is comprised of numerous knots and filaments. The hidden AGN is thought to be 0''.3 south of the optical continuum peak (Capetti et al. 1997), AKA the “Hot Spot” (Kraemer & Crenshaw 2000b).

Optical and UV spectra of NGC 1068, in particular those obtained with the Space Telescope

---

<sup>1</sup>The NASA/IPAC Extragalactic Database (NED) is operated by the Jet Propulsion Laboratory, California Institute of Technology, under contract with the National Aeronautics and Space Administration

Imaging Spectrograph aboard *HST*, have been studied in detail (e.g., Crenshaw & Kraemer 2000a,b; Kraemer & Crenshaw 2000a,b). The optical emission is dominated by the Hot Spot, spectra of which show emission lines from an extreme range of ionization, e.g., [O I]  $\lambda 6300$  to [Fe XIV]  $\lambda 5303$  and [S XII]  $\lambda 7611$ ; the latter two are likely the footprint of the X-ray emission line gas. The Hot Spot is also a source of strong scattered continuum radiation. Within  $\sim 200$  pc, on either side of the nucleus, the gas is somewhat less highly ionized, however strong N V  $\lambda 1240$ , C IV  $\lambda 1550$ , and [Ne V]  $\lambda 3426$  are still present. Photoionization modeling has shown that the gas is ionized by the continuum radiation from the central source, although there are localized regions which show evidence for enhanced ionization due to shocks.

Both red- and blue-shifted emission lines are present on either side of the nucleus (Crenshaw & Kraemer 2000b). Based on kinematic modeling (Das et al. 2006), the observed velocities result from outflow along a hollow bicone, with a half opening angle of  $40^\circ$ . The axis of the bicone is inclined  $5^\circ$  with respect to the plane of the sky, with the NE side pointed towards the observer, which is consistent with the morphology of the H I 21 cm emission (Gallimore et al. 1994). The maximum de-projected outflow velocity is  $\sim 2000$  km s $^{-1}$  with a peak  $\sim 140$  pc from the central nucleus, after which there is rapid deceleration to systemic. Although outflowing, photoionized gas is suggestive of radiative acceleration, the velocity profiles are not fully consistent with any simple form of AGN-driven flow (Das et al. 2007; Everett & Murray 2007). The main issue is that the flow appears to accelerate much more gradually than predicted. One possibility is mass loading, perhaps in the form of interaction with more tenuous ambient gas.

Absorption of the 2–10 keV X-ray continuum in Type 1 AGN by photoionized gas (now generally referred to as “warm absorbers”) was first suggested by Halpern (1984). Although modification of the X-ray continuum by the absorber could account for the overall spectral properties of such sources, *ASCA* spectra of Seyfert 1 galaxies revealed evidence for an unabsorbed component of emission (George et al. 1998), particularly in the soft X-ray band (energies  $< 1$  keV). In their analysis of these, George et al. (1998) found that, in many cases, the fit statistics improved when a component of unabsorbed emission-line gas was included. In fact, Netzer (1993, 1996) had predicted that there would be strong soft-X-ray emission lines associated with warm absorbers.

The unprecedented X-ray spectral resolution afforded by the *XMM-Newton* (hereafter *XMM*) Reflection Grating Spectrometer (RGS) and the *Chandra*/ High Energy Transmission Grating (HETG) and Low Energy Transmission Grating (LETG) have revealed the myriad of emission lines predicted by Netzer (1993). Furthermore, based on *Chandra*/HETG observations, Ogle et al. (2000) found extended soft X-ray emission in the Seyfert 1 galaxy,

NGC 4151. As it is roughly spatially coincident with the optical [O III] emission and radio continuum, it likely arises in the NLR. Similarly, the NLR is the source of the soft X-ray emission in Seyfert 2 galaxies. For example, X-ray observations of NGC 1068 show an extended region of soft X-ray emitting gas, broadly coincident with the [O III] bicone (Young et al. 2001; Ogle et al. 2003). The extended emission component likely has contributions from both line emission and a small electron-scattered component of the X-ray continuum.

Previous analyses, based upon RGS (Kinkhabwala et al. 2002) and *Chandra*/LETG (Brinkman et al. 2002) and HETG (Ogle et al. 2003) observations have revealed a multitude of emission lines in NGC 1068. Particularly prominent are strong H- and He-like lines of C, N and O. These are accompanied by weaker highly-ionized lines from Ne, Mg, Si, S and Fe. Via its superior spatial resolution, the *Chandra* observations revealed two peaks of X-ray emission, one centered on the nucleus and the other  $3''$  -  $4''$  to the NE. The overall emission-line spectra was found to be similar in both regions (Brinkman et al. 2002; Ogle et al. 2003). Ogle et al. (2003) suggested that the X-ray emission-line was the source of the scattered optical continuum, detected via spectro-polarimetry (Miller et al. 1991). Consideration of the ensemble of line measurements has suggested that both photoionization and photoexcitation are important ionization processes for the X-ray emitter (Kinkhabwala et al. 2002; Ogle et al. 2003), with no clear evidence of a collisionally ionized component. However, none of these authors generated detailed photoionization models to analyze the physical properties of the emission-line gas.

More recently, Kallman et al. (2014) analyzed a 450 ksec *Chandra*/HETG spectrum of NGC 1068, using photoionization models generated with the code XSTAR (Kallman et al. 2004). Overall, their results support the claims in Kinkhabwala et al. (2002) and Ogle et al. (2003), specifically that the emission-line gas is photoionized, with some evidence for photoexcitation, and the emission-lines are blue-shifted, indicative of outflows. They found that multiple zones, characterized by a range of ionization parameters and column densities were required to match the measured emission line fluxes. Furthermore, in order to fit the spectra, they allowed the oxygen and iron abundances to vary among the components. However, *Chandra*/Medium Energy Grating has a low effective area at wavelengths  $> 25 \text{ \AA}$ . As a result, Kallman et al. (2014) were unable to compare the oxygen lines to many of the strong lines of nitrogen and none of carbon, and therefore they were unable to determine how their assumed abundances might result within the constraints of nucleosynthesis models. We will revisit these points in Section 3.

In this paper we re-investigate the soft X-ray spectra obtained using the RGS in the context of photoionization models generated with CLOUDY (Ferland et al. 1998). The goals of our study include a reassessment of the physical processes responsible for ionizing the X-ray gas

and a better understanding of the relationship between the X-ray emitter and other key components of the nuclear outflow. Progress on these questions will, in turn, lead to a better understanding of the energy and material transport between the active nucleus and the host galaxy.

## 2. Observations and Data Analysis

The observation of NGC 1068 reported here was made by *XMM* on 2000 July 29 - 30 (OBSIDs 011100101, 0111200201). The standard RGS and PN data products were extracted from the archive, having been produced by the *XMM* Science Analysis Software (SAS) v6.6.0. The RGS offers a useful bandpass  $\sim 0.4 - 2.0$  keV ( $\sim 6 - 31\text{\AA}$ ). Due to the failure of RGS1 CCD7 and RGS2 CCD4 (soon after launch), there are no useful data over the wavelength range 11-14  $\text{\AA}$  (0.9-1.2 keV) and 20-24  $\text{\AA}$  (0.51-0.62 keV) for RGS1 and RGS2, respectively. Subsequent reprocessing and analysis were performed using a more recent version of SAS<sup>2</sup> (v10.0.0) and various tasks from the HEASOFT<sup>3</sup> (v6.9) software suite.

In order to determine the RGS wavelength scale the position of the zeroth order must be determined. This is not possible using the RGS instrument alone. Thus, we used the *HEASoft* "xrtcentroid" task (within XIMAGE v0.2.9) to determine the centroid of the image from the co-aligned PN instrument in the RGS wavelength band. The centroid position was found to be at RA =  $02^{\text{h}}42^{\text{m}}40.70^{\text{s}}$ , DEC =  $-0^{\circ}00'46.24''$  (J2000). We estimated the uncertainty of our centroid position to be  $1.5''$  based upon repeated trials of the task, i.e., less than one image pixel ( $1.6''$  on a side). Our X-ray centroid position is consistent with that derived from *Chandra* observations of the source (Young et al. 2001) but is  $\sim 6.3''$  away from the position assumed in the (SAS v6.6.0) processing of the RGS data that created the archived data products. (The processing software uses the position supplied by the principal investigator). We also note that our centroid position is  $\sim 5''$  away from the X-ray centroid position determined by Kinkhabwala et al. (2002) for this *XMM* observation, attributable to improvements in attitude determination software between the original processing of the data and the current archived version. As the RGS energy scale is determined by the angle a photon has been dispersed relative to the zeroth order position, this difference in attitude solution does not affect the line energy determination relative to that performed by Kinkhabwala et al. (2002). Further to the uncertainty on photon energy related to the statistical uncertainty in determination of the centroid and therefore the dispersion angle,

---

<sup>2</sup><http://xmm.esac.esa.int/sas/>

<sup>3</sup><http://heasarc.gsfc.nasa.gov/docs/software/lheasoft.html>

there is an additional uncertainty in the absolute energy scale that corresponds to a  $1\sigma$  uncertainty in velocity of  $105 \text{ km s}^{-1}$  at  $20\text{\AA}$ .

Given the above, we reprocessed the RGS data from both OBSIDs using SAS v10.0.0 to produce co-added source and background spectra for each RGS, based on our X-ray centroid position. The total exposure times were 84.7 ks and 82.5 ks for RGS 1 and 2 respectively. The mean source count rates (in the 0.4-2 keV band) were  $0.568 \pm 0.003 \text{ cts/s}$  and  $0.516 \pm 0.003 \text{ cts/s}$  for RGS 1 and RGS 2 respectively. The background comprised  $\sim 20\%$  of the total count rate.

## 2.1. Spectral Analysis

### 2.1.1. Initial Line Fitting

The source spectral (without background subtraction), background and response files obtained after reprocessing the data (as discussed above), were loaded into XSPEC (Arnaud 2010) to create the background-subtracted source spectra from RGS 1 and 2, as shown in Figure 1 (*orange* color). This methodology allows XSPEC to perform the background subtraction and preserve the full statistical information from the data. The RGS spectra contained  $> 10$  counts in most of the channel range used allowing us to utilize the  $\chi^2$  statistic for fitting.

Inspection of the spectra revealed several prominent lines (Figure 1) including those from H-like and He-like transitions of O, C, N, Ne, Mg and Si. Of particular interest are the very prominent triplets that arise from He-like species, such as N VI, O VII and Ne IX, that can yield constraints on the gas density and excitation mechanism (Porquet & Dubau 2002).

To extract the parameters for these lines, narrow sections of the data were fit using XSPEC. As far as was possible, the lines were isolated (by ignoring data around the selected range) and fit individually such that each line could be fit accurately. Each line profile was modeled using a Gaussian component whose flux, width and energy were allowed to vary (Table 1). The Galactic column density was accounted for in the spectral analysis by using the neutral absorption model TBABS (Wilms et al. 2000). The column density for the TBABS component was allowed to vary between  $2.92 \times 10^{20} \text{ cm}^{-2}$  (Dickey & Lockman 1990) and  $3.53 \times 10^{20} \text{ cm}^{-2}$  (Kalberla et al. 2005), to account for the uncertainty in this quantity. The best-fit value of the Galactic column pegged at the high end of this range in the fit and, therefore was initially fixed at  $3.53 \times 10^{20} \text{ cm}^{-2}$  (but see Section 3.2.1). The continuum close to each line was fit with a power-law component that was allowed to vary. The best fit line parameters



are detailed in Table 1 for lines above the threshold of observed flux  $> 10^{-6}$  photons  $\text{cm}^{-2} \text{s}^{-1}$ . We tabulated  $1\sigma$  errors on each parameter (i.e., calculated at 68% confidence).

As expected, our measured emission-line fluxes are in good agreement with those of Kinkhabwala et al. (2002). However, the RGS fluxes are  $\sim 2$  greater than those measured in *Chandra*/HETG spectra (Ogle et al. 2003; Kallman et al. 2014). The difference is due to the much larger extraction region for the RGS. To illustrate this, in Figure 2 we show the RGS and *Chandra*/HETG extraction windows, overlaid on a *Chandra*/ACIS image. Clearly, much of the X-ray emission-line region is outside the *Chandra* window.

Fe M- and L-shell transitions (Fe XIV to Fe XXIV) are heavily blended with H- and He - like lines of Ne (Figure 1), therefore the strengths of these lines could not be usefully constrained. The higher-order transition lines of Mg, Si and S are barely resolved due to the low sensitivity of the RGS in the wavelength regime (6-10 Å).

### 2.1.2. Kinematics

We have identified the observed lines using the expected laboratory energies from the National Institute of Standards and Technology (NIST), supplemented by the Kentucky atomic database (Table 2). Most of the emission lines show a significant blue-shift relative to the host galaxy ( $cz = 1137 \pm 3$  km/s; Huchra et al. 1999), indicating an origin in outflowing gas, as previously found by other authors (e.g. Kinkhabwala et al. 2002). Based on the strongest, most isolated lines from He-like N and O and H-like C, N, and O, there is evidence for two kinematic components, with the N VI and O VII *f* lines having more negative radial velocities than the N VII and O VIII Ly $\alpha$  lines (See Figure 3). However, the velocities of the latter are consistent with those of the N VI and O VII *r* lines, within the uncertainties. Unfortunately, the Ne IX and Ne X lines are weaker and heavily blended with Fe lines, hence it is impossible to see if the same trend is present. Overall, the radial velocities are on the same order as that measured for [O III]  $\lambda 5007$ ,  $v_{\text{rad}} \sim 160$  km  $\text{s}^{-1}$  (Crenshaw et al. 2010b), which suggests that the X-ray and optical emission-line gas have similar kinematics. Note that these velocities are not de-projected and the actual outflows may be much faster (e.g. Das et al. 2006). As we also note in Section 3.2.1, while the kinematics are *consistent* with distinct low and high ionization zones, their radial velocities cannot be well constrained with these data.

Velocity widths (*FWHM*) were determinable for a few strong lines (Table 2). The strongest lines, e.g., N VI *f* and O VII *f* are resolved using RGS, with velocity widths  $FWHM \approx 926$

and  $\approx 1003 \text{ km s}^{-1}$ , respectively<sup>4</sup>. This is quite close to the value measured for [O III]  $\lambda 5007$ ,  $FWHM \approx 1060 \text{ km s}^{-1}$  (Whittle 1992), again indicative of similar kinematics for the X-ray and optical emission line gas. The values are in excess of the radial velocities and most likely result from the superposition of different kinematic components along our line-of-sight.

### 3. Photoionization Modeling

#### 3.1. Inputs to the Models

Previous analyses for the soft X-ray emitting gas in NGC 1068 have used selected line measurements to explore the conditions in the emitting gas (Kinkhabwala et al. 2002). Here we aim to construct a self-consistent photoionization model for the X-ray emitter. To this end, we have made use of the photoionization code, CLOUDY version C10.00, last described by Ferland et al. (2013). As usual, our model results depend on the choice of input parameters, specifically: the spectral shape of the incident radiation or spectral energy distribution (SED), the radial distances of the emission-line gas with respect to the central source, the number density of atomic hydrogen ( $n_{\text{H}}$ ) and column density ( $N_{\text{H}}$ ) of the gas, and its chemical composition. Given the large radial distances ( $> 10\text{s}$  of pc) of the emission-line gas, we have assumed open, or slab-like, geometry. The models are parameterized in terms of the dimensionless ionization parameter  $U$ , the ratio of ionizing photons per nucleon at the illuminated face of the slab, or:

$$U = \frac{Q}{4\pi R^2 c n_{\text{H}}} \quad (1)$$

where,  $R$  is the distance to the continuum source,  $c$  is the speed of light, and the total number of Lyman-continuum photons  $\text{sec}^{-1}$   $Q = \int_{13.6\text{eV}}^{\infty} \frac{L_{\nu}}{h\nu} d\nu$ , emitted by a source of luminosity  $L_{\nu}$ .

##### 3.1.1. The Ionizing Continuum

We assumed an SED in the form of a broken power law  $F_{\nu} = K \nu^{-\alpha}$ , with  $\alpha = 1.0$  below 13.6 eV,  $\alpha = 1.7$  from 13.6 eV to 0.5 keV, and  $\alpha = 0.8$  from 0.5 keV to 30 keV

---

<sup>4</sup>The RGS FWHMs at these wavelengths, linearly extrapolating between the values at  $35.4\text{\AA}$  and  $15.5\text{\AA}$ , are  $775 \text{ km s}^{-1}$  and  $1000 \text{ km s}^{-1}$



(Kraemer & Crenshaw 2000b), where  $\alpha$  is the energy index. We also included a low energy cut-off at 1 eV and a high energy cutoff at 100 keV.

Since our view of the central source is blocked in NGC 1068, we estimated the ionizing luminosity using an “isotropic” quantity, specifically the [O IV] 25.89  $\mu\text{m}$  emission line (see Meléndez et al. (2008)). The [O IV] flux, detected with the *Infrared Space Observatory*-Short Wave Spectrometer, is approximately  $1.9 \times 10^{-11} \text{ ergs cm}^{-2} \text{ s}^{-1}$  (Lutz et al. 2000), which corresponds to a line luminosity  $L_{\text{OIV}} \approx 10^{41.53} \text{ ergs s}^{-1}$ . Using the linear regression fit to  $L_{\text{OIV}}$  and the 2-10 keV ( $L_{2-10\text{keV}}$ ) luminosity for Seyfert 1 galaxies calculated by Meléndez et al. (2008), we estimate  $L_{2-10\text{keV}} \sim 10^{43.8} \text{ ergs s}^{-1}$ , which, for a bolometric correction of  $\sim 30$  (Awaki et al. 2001), yields  $L_{\text{bol}} \sim 10^{45.3} \text{ ergs s}^{-1}$ . The corresponding mass accretion rate is  $\dot{M} = L_{\text{bol}}/\eta c^2$ , or  $0.35 \text{ M}_{\odot} \text{ yr}^{-1}$ , for  $\eta = 0.1$ . Interestingly, given a black hole mass of  $1.5 \times 10^7 \text{ M}_{\odot}$  (Greenhill & Gwinn 1997), the central source is radiating at approximately its Eddington limit. Based on these values and our assumed SED, we find the ionizing luminosity  $L_{\text{ion}} \sim 10^{44.2} \text{ ergs s}^{-1}$  and  $Q \sim 10^{54.4} \text{ photons s}^{-1}$ .

### 3.1.2. Elemental Abundances

Our initial approach was to find an approximate solution for the gas by comparing the ratio of intensities of selected strong emission lines in the data with those predicted by the CLOUDY model. The line ratios selected were for the strengths of H-like and He-like ions relative to O VII  $f \lambda 22.10 \text{ \AA}$  (the latter was selected by virtue of being the strongest line detected in the RGS data), similar to the approach used in the analysis of the RGS spectrum of the Seyfert 1 galaxy NGC 4151 by Armentrout et al. (2007). We first generated CLOUDY photoionization models assuming solar abundances (Grevesse & Sauval 1998). This initial comparison revealed no single-zone gas solution that could adequately describe the observed line ratios. Specifically, models with solar abundances over-predicted the strongest oxygen lines, OVII  $f \lambda 22.10 \text{ \AA}$  and O VIII  $\text{Ly}\alpha$ , relative to the lines from other abundant elements/ions, in particular, and He-like carbon and nitrogen. Interestingly, in photoionized gas the X-ray emission lines from second-row elements are primarily produced by recombination or, for permitted transitions if the lines are optically thin, by photoexcitation. The other strong features in the RGS spectrum include radiative recombination continua (RRCs) which are obviously formed via recombination. Hence, the strengths of these features are quite sensitive to relative elemental abundances. Notably, it has been argued that optical and UV recombination lines are more reliable indicators of elemental abundances than collisionally excited forbidden lines, which are typically used to estimate elemental abundances in optical spectra, due to the sensitivity of the latter on temperature and density fluctuations (Peimbert 1967).

In the analysis of RGS spectra of the Seyfert 1 NGC 3516, Turner et al. (2003) found that the model fit was improved by assuming both super-solar N/O and sub-solar C/O abundance ratios. They argued that this was consistent with conversion of carbon to nitrogen via the CNO-cycle in intermediate mass stars ( $M \leq 7 M_{\odot}$ ; e.g. Maeder & Meynet (1989)), and that fairly large N/O ratios, e.g., a few times solar, could occur in stars with initially roughly solar abundances. However, the NGC 1068 spectra also show strong carbon lines (see Fig. 1), which are not consistent with the loss of carbon, at least if the overall abundances were approximately solar. In studies of H II regions in the Milky Way, evidence has been found for a C/O gradient, with a C/O ratio  $\sim$  unity, while O/H ratio was roughly solar, at radial distances  $\lesssim 7$  kpc (e.g. Esteban et al. 2005). The enhancement of carbon in the Milky Way interstellar medium could be due to either stellar winds from massive stars,  $8 \leq M/M_{\odot} \leq 80$  (Henry et al. 2000), or a combination of high-metallicity massive stars and low-metallicity low-to-intermediate mass stars,  $0.8 \leq M/M_{\odot} \leq 8$  (Carigi et al. 2005). In either case, if the carbon were significantly enhanced in a star with otherwise solar abundances, the conversion of carbon-to-nitrogen described above could lead to both high C/O and N/O ratios while O/H evolved as  $Z/Z_{\odot}$ . Based on this, we assumed that metallicities of pro-genitor stars were solar (Asplund et al. 2005), although with C/O approximately  $3 \times$  solar, as compared to the roughly twice solar values found by Esteban et al. (2005). We further assumed that nucleosynthesis brings the overall metallicity to  $1.5 \times$  solar, but with all the added carbon going into the production of nitrogen. The resulting abundances, with the log values, relative to H by number, are as follows: He:  $-0.83$ ; C:  $-3.06$ ; N:  $-3.36$ ; O:  $-3.13$ ; Ne:  $-3.90$ ; Na:  $-5.59$ ; Mg:  $-4.23$ ; Al:  $-5.39$ ; Si:  $-4.32$ ; P:  $-6.42$ ; S:  $-4.71$ ; Ar:  $-5.43$ ; Ca:  $-5.49$ ; Fe:  $-4.33$ ; and Ni:  $-5.61$ . Here the N/H and C/H ratios are  $6$  and  $3.2 \times$  solar, respectively, while the other heavy element abundance ratios are  $1.5 \times$  solar. It should be noted that Brinkman et al. (2002) suggested super-solar nitrogen abundance and Kallman et al. (2014) required non-solar heavy element abundances for their photoionization models. Based on the strong C and Fe emission in the RGS spectra, there is no evidence for depletion of these elements onto dust grains. Therefore we did not include cosmic dust in the models.

### 3.2. Spectral fitting results

The range in ionization states detected in these spectra suggests the presence of two distinct components of emission-line gas, therefore our approach was to generate two model grids with CLOUDY. Consideration of the ratio  $\frac{NVI}{OVII}$  and  $\frac{NeX}{OVIII}$  suggested that these zones lie in the ranges  $\log U \sim -1$  to  $0$ ,  $\log N_H \sim 20 - 22$  and  $\log U \sim 0 - 2$ ,  $\log N_H \sim 20 - 23$ .

### 3.2.1. The Final Model

To refine our solution, the RGS spectra were compared to a model comprising two ‘candidate’ model zones. Based upon the initial results from the line ratio analysis, we re-ran CLOUDY with model step intervals of 0.1 in the log of  $U$  and  $N_{\text{H}}$ , across the ranges  $-2 < \log U < 2$  and  $20 < \log N_{\text{H}} < 24$ , using the elemental abundances noted above. Initially, the resonance lines of the He-like triplets (only) were underpredicted compared to the forbidden lines. Thus, to boost the strength of these resonance lines, we included micro-turbulence of 35 km s<sup>-1</sup>. This corresponds to a  $FWHM = 82$  km s<sup>-1</sup>, which is significantly less than that of the resolved lines discussed in Section 2.1.2, which likely result from the superposition of kinematic components along our line of sight. Following Porter et al. (2006), we then created a FITS format ATABLE from the CLOUDY output. To facilitate a comparison of the model tables with the ensemble of line results we performed spectral fitting of the RGS data using our ATABLE.

Our final model was comprised of two zones (LOWION and HIGHION), each absorbed by the Galactic line-of-sight column density, parameterized using TBABS. The value of TBABS was initially set to  $N_{\text{H}} = 3.53 \times 10^{20} \text{cm}^{-2}$  (Kalberla et al. 2005), but in the final fit the value was allowed to vary. Fitting the model to the data showed the model lines to be systematically too narrow to account for the observed line ensemble. Therefore we smoothed the model spectra using a Gaussian function equivalent to  $\sigma = 365$  km s<sup>-1</sup> ( $FWHM = 852$  km s<sup>-1</sup>) for LOWION and  $\sigma = 1170$  km s<sup>-1</sup> ( $FWHM = 2732$  km s<sup>-1</sup>) for HIGHION. The LOWION smoothing is consistent with the measured widths for N VI  $f$  and O VII  $f$  (see above). The fitting was allowed to proceed until the reduced  $\chi^2$  was minimized; the final model parameters are listed in Table 3. In the process, the outflow velocities for LOWION and HIGHION converged on values of 215 km s<sup>-1</sup> and 166 km s<sup>-1</sup>, respectively. However, these values overlap within the uncertainties, as suggested in Section 2.1.2. Also, the fitting returned a Galactic column of  $5.43^{+0.44}_{-0.28} \times 10^{20} \text{cm}^{-2}$ , somewhat larger than the value from Kalberla et al. (2005). However, there is evidence for absorption by low-ionization gas covering the NLR of NGC 1068 (see Kraemer & Crenshaw 2000b; Kraemer et al. 2011), and it is plausible that the extra column of neutral gas is associated with that.

As shown in Figure 1, we obtained a reasonable (i.e., reduced  $\chi^2 = 1.99$ ) fit to the data with two components, the relative contributions of which are shown in Figure 4. The contributions to  $\chi^2$  are shown in Figure 5, which illustrates that most of the mismatch to the data is due to under-predicted emission below 17Å. In order to determine and compare the predicted emission line fluxes to the intrinsic line luminosity, which is necessary to determine the covering factors of the emission-line gas,  $n_{\text{H}}$  must be determined for each component, which requires fixing their radial distances. For the sake of simplicity, we assumed that LOWION

and HIGHION are co-located. As a reference point, we assume they are at a distance  $R = 50$  pc from the central source, which is consistent with the fact that most of the X-ray emission arises within the central  $\sim 100$  pc (see Ogle et al. 2003). Note that the X-ray emission-line ratios are not sensitive to density over the range expected for X-ray emitters in the NLR (e.g.,  $< 10^6 \text{ cm}^{-3}$ ; Porquet & Dubau 2002). Also, we do not have any strong constraints of the location of the emission-line gas, except that the emission is centrally peaked. However, this distance is reasonable given the distribution of scattered continuum (Crenshaw & Kraemer 2000a) and the probability that much of the emission from the inner 30 pc is heavily attenuated (e.g., Kraemer & Crenshaw 2000a; Kraemer et al. 2011). Using the value of  $Q$  derived in Section 3.1.1, we obtain  $n_{\text{H}} = 15 \text{ cm}^{-3}$  and  $265 \text{ cm}^{-3}$  for HIGHION and LOWION, respectively. One additional check on whether the models are physically plausible is the requirement that the depth of the model,  $\Delta R = N_{\text{H}}/n_{\text{H}}$ , is less than the components radial distance,  $R$  (e.g. Blustin et al. 2005; Crenshaw & Kraemer 2012). For these model parameters,  $\Delta R/R = 0.02$  and  $0.68$  for LOWION and HIGHION, respectively.

Based on the fitting, LOWION and HIGHION contribute 0.96 and 0.04 of O VII-f and 0.14 and 0.86 of O VIII Ly- $\alpha$ , respectively. Using these fractional contributions, we computed the predicted emission-line fluxes from each component and the total flux. The former are computed by comparing the predicted O VII-f and O VIII Ly- $\alpha$  fluxes to the absorption-corrected fluxes, taking into account the fractional contributions of each component, in order to derive a scaling factor for each component. Then the remaining line fluxes are computed by multiplying the ratios of their fluxes to those of O VII-f or O VIII Ly- $\alpha$  by the derived scaling factors. The final values are listed in Table 1, along with the observed and absorption-corrected fluxes. The fits for the individual lines are good overall, with the predictions for most of the stronger lines (i.e., with fluxes  $\gtrsim 3 \times 10^{-4} \text{ photon cm}^{-2} \text{ s}^{-1}$ ) within  $\sim 30\%$  of the absorption-corrected values. The discrepancies include C v He $\beta$  and He $\delta$ , which are relatively weak and in a region where determining the continuum level is non-trivial and N VII Ly- $\alpha$  is somewhat under-predicted.

In addition to emission lines included in Table 1, we also compared the predicted and measured RRCs, using the same relative contributions from the two model components (see Table 4). Although we detected the O VIII RRC, the feature is too heavily blended with the surrounding emission for us to have been able to determine the width and flux accurately. Overall, the predicted fluxes fit the measured values reasonably well. The model-predicted electron temperatures correspond to widths of  $kT = 4.0 \text{ eV}$  and  $44.4 \text{ eV}$ , for LOWION and HIGHION, respectively. While the LOWION value is on the same order as the measured values of the He-like RRCs, the HIGHION prediction is several times that of the measured H-like RRCs. This is likely the result of the difficulty in fitting these broader features. How-

ever, both the models and data confirm that the emission-line gas possesses temperatures consistent with photoionization.

As noted above, the greatest mismatch between the model and the data is in the region 10-17 Å, which shows a heavy blend of emission lines of Fe XIV-XXIV with those from Ne IX, Ne X, and O VIII (for a more complete identification of the iron lines see Kinkhabwala et al. 2002). HIGHION predicts that the maximum ionization states of iron are spread from Fe XVII to Fe XXI, within the observed range, however the predicted line fluxes are quite weak and essentially make a negligible contribution to the model spectrum (see Figure 4). The underprediction may be the result of the incomplete atomic data for iron, specifically rates for fluorescence following inner shell ionization.

### 3.2.2. Model-derived Covering Factors

Having obtained a reasonable fit to the RGS spectrum with our two component model, we calculate the covering factors ( $C_f$ ) for each component by comparing the emitting area, the ratio of the emission-line luminosities to their model-predicted fluxes, to the surface area of a sphere surrounding the central source. As we mentioned above, we assume that both LOWION and HIGHION are 50 pc from the source, which sets  $n_H$  for each component for the value of  $U$  for each component, and thus the predicted emission line-fluxes. Based on our spectral fitting, the total luminosity of the O VII-f line emitted by LOWION is  $\sim 2.5 \times 10^{40}$  ergs s $^{-1}$ . Dividing by the predicted flux, 0.215 ergs cm $^{-2}$  s $^{-1}$ , the total emitting surface area of LOWION is  $\sim 10^{41}$  cm $^2$ , which corresponds to a covering factor  $C_f = 0.35$ . Based again on our spectral fitting, for HIGHION, the total luminosity of O VIII Ly $\alpha$  is  $\sim 1.5 \times 10^{40}$  ergs s $^{-1}$ , while the predicted flux is 0.051 ergs cm $^{-2}$  s $^{-1}$ , from which we derive an emitting surface of  $2.5 \times 10^{41}$  cm $^2$  and  $C_f = 0.84$ . Although the covering factors are physically possible, in the sense that they are less than unity, the value for HIGHION requires that this component subtends a larger solid angle than the emission-line bicone, even if the bicone were filled (e.g. Das et al. 2006). We will revisit this point in Section 4.3.

### 3.2.3. UV and Optical Constraints on the X-ray Emission-Line Gas

Although the ionization parameters for both emission components are significantly higher than those determined for the UV and optical emission-line gas (e.g. Kraemer et al. 1998; Kraemer & Crenshaw 2000b), except for the “CORONAL” component of the Hot Spot (Kraemer & Crenshaw 2000a), the LOWION model predicts strong O VI  $\lambda\lambda$  1031.9, 1037.6. Scaling the predicted flux by the emitting area determined from the O VII f-line, the pre-

dicted O VI luminosity is  $\sim 1.9 \times 10^{41}$  ergs s $^{-1}$ , which corresponds to an observed flux  $F_{OVI} \sim 1.0 \times 10^{-11}$  ergs cm $^{-2}$  s $^{-1}$  (note that the contribution from HIGHION is more than two orders of magnitude less, hence can be ignored).

NGC 1068 was observed with the Hopkins UltraViolet Telescope (HUT), aboard the space shuttle Columbia (Kriss et al. 1992), through two circular apertures of 18'' and 30'', hence encompassing the region of strong X-ray emission (e.g. Young et al. 2001). They measured  $F_{OVI} = 3.74 (\pm 3.1) \times 10^{-12}$  ergs cm $^{-2}$  s $^{-1}$ . While the emission-line fluxes reported by Kriss et al. were not corrected for extinction, based on the the ratio of He II  $\lambda 1640$  (from HUT) to He II  $\lambda 4686$  (Koski 1978), they derived an extinction  $E_{B-V} = 0.16$ , assuming an intrinsic 1640/4686 ratio of 7.0 (Seaton 1978). Using the UV extinction curve in Seaton (1979), the corrected  $F_{OVI} \approx 2.5 \times 10^{-11}$  ergs cm $^{-2}$  s $^{-1}$ , which indicates that LOWION contributes 40% of the O VI emission. Based on this, our model meets the constraints from the UV emission. Also, it is possible that some regions of UV and optical emission are undetectable due to extinction (see discussion in Kraemer et al. 2011), but could be detected in the X-ray, in which case LOWION accounts for an even smaller fraction of the intrinsic UV emission.

Given the model parameters of the Hot Spot CORONAL component ( $\text{Log}U = 0.23$ ;  $\log N_H = 22.6$ ; Kraemer & Crenshaw 2000a), it could contribute to the overall X-ray emission. However, neither of our components have similar parameters. Furthermore, while CORONAL was optimized to match the observed [S XII]  $\lambda 7611$ , the peak ionization states are S IX and S XV for LOWION and HIGHION, respectively. Finally, forcing the inclusion of a component similar to CORONAL into the spectral fitting produced statistically unacceptable results. This suggests that the conditions that give rise to the [S XII] emission are not typical of the X-ray NLR as a whole.

## 4. Discussion

### 4.1. Total Mass and Mass Loss Rates

Based on our model results and constraints on the covering factors of each component, we can determine the total mass of the X-ray emission-line gas,  $M_{\text{tot}}$ , for a given radial distance,  $R$ . Assuming the gas lies in shells, the thickness of which are constrained by the model-derived values of  $N_H$ , the total mass is given by:

$$M_{\text{tot}} = 4\pi R^2 N_H \mu m_p C_f \quad (2)$$



where  $m_p$  is the mass of a proton and the factor  $\mu$  is the mean atomic mass per proton (we assume  $\mu = 1.4$ , primarily from the contribution from helium). For our fiducial distance,  $R = 50\text{pc}$ , and derived model parameters, we obtain  $M_{\text{tot}} = 8.7 \times 10^4 M_\odot$  and  $4.7 \times 10^5 M_\odot$  for LOWION and HIGHION, respectively. Note, given the possibility that the emission-line gas lies at greater radial distance,  $M_{\text{tot}}$  could be somewhat greater.

We estimate the mass loss rates,  $\dot{M}$ , as follows (Crenshaw et al. 2003):

$$\dot{M} = 4\pi R N_H \mu m_p C_f v \quad (3)$$

where  $v$  is the outflow velocity. Using  $v_{\text{rad}}$  in place of  $v$ , we obtain mass loss rates of  $\dot{M} \sim 0.38 M_\odot \text{ yr}^{-1}$  and  $0.06 M_\odot \text{ yr}^{-1}$  for the two components. Clearly,  $\dot{M}$  would be greater if the gas were at a larger radial distance, as is the case for  $M_{\text{tot}}$ , or if the outflow velocities were greater than  $v_r$ .

The derived values of  $M_{\text{tot}}$  and  $\dot{M}$  are roughly the same as those determined from the *Chandra*/HETG spectrum by Kallman et al. (2014), and, based on our estimate of  $L_{\text{bol}}$ , the latter is on the same order as that of the fueling rate. From the results of the STIS long slit spectral analysis (Kraemer & Crenshaw 2000a,b), we estimate that within a single slit position, at PA202°, the total amount of emission-line gas is  $\sim 6 \times 10^3 M_\odot$ . Scaling this quantity by the ratio of the dereddened [O III]  $\lambda 5007$  flux from the STIS spectra and the [O III] flux in ground-based spectra (Bonatto & Pastoriza 1997), dereddened as per the discussion in Section 3.2.3, we estimate a total mass of the optical emission-line gas of  $\sim 3.8 \times 10^4 M_\odot$ . This is on the same order mass of ionized gas determined from spectra obtained with the *Gemini*/Near-Infrared Field Spectrograph by Riffel et al. (2014), hence it is unlikely that we have grossly underestimated the mass of optical emission-line, due to regions of heavy extinction (e.g. Kraemer et al. 2011). Therefore, these results indicate that the X-ray emission-line gas is a major, if not dominant, component of ionized gas in the NLR.

## 4.2. Thermal and Pressure Stability

The predicted gas pressures at the ionized faces of LOWION and HIGHION are  $4.3 \times 10^{-9} \text{ dyn cm}^{-2}$  and  $2.7 \times 10^{-9} \text{ dyn cm}^{-2}$ , respectively, which indicate that, given uncertainties in the model parameters, these components are roughly in pressure equilibrium if co-located. In contrast, the predicted gas pressure for the UV/optical emission-line gas from the Hot Spot is  $3.5 \times 10^{-7} \text{ dyn cm}^{-2}$  (based on the model parameters in Kraemer & Crenshaw 2000a). Therefore, UV/optical knots would not be pressure-confined by the X-ray emission-line gas. In that case, one would expect to see a drop in the density of the optical/UV gas with radial



distance. However, given the large pressure differential, the density drop would be much more rapid than observed (Kraemer & Crenshaw 2000b). This suggests other scenarios, such as creation/evaporation of clouds out of/into the X-ray medium (Krolik & Kriss 2001) or in situ acceleration of gas that has rotated into the illumination cone (Crenshaw et al. 2010a), rather than outflow and expansion of individual knots.

In Figure 6 we show the  $\log T - \log U/T$ , or S-Curve, plot generated with our assumed SED and abundances. Note that there is only one region with pronounced negative slopes, indicative of strong instabilities; the overall stability is the result of the high metal abundances in our models (see Bottorff et al. 2000). The insert shows that both components lie on stable, i.e., positive-sloped sections of the S-curve. While HIGHION does lie close to an unstable region, given that the AGN is radiating close to its Eddington limit, it is unlikely that it will experience an ionizing flux increase that would drive it into instability.

### 4.3. Structure of the X-ray NLR

As noted in Section 3.2.2, the model-derived covering factors are physically possible. However, it is difficult to reconcile such large values considering that the optical emission SW of the nucleus is heavily attenuated by the disk of the host galaxy (Kraemer & Crenshaw 2000a) and that X-ray emission from the inner  $\sim 30$  pc appears to be absorbed by gas outside the bicone (Kraemer et al. 2011). Hence, it is likely that there is more X-ray emission line gas than that detected in the RGS spectra. If so, the covering factors could be significantly greater and could easily exceed unity for HIGHION.

Both HIGHION and LOWION are matter-bounded and, in such cases, emission-line fluxes can be increased to an extent by increasing  $N_H$ . This would, correspondingly, decrease the required emitting surface areas and, hence, the covering factors. However, in the case of HIGHION,  $N_H$  is constrained by the  $\Delta R/R$  condition (see Section 3.2.1). One way around this is if the emission-line gas consists of a number of matter-bounded components at increasing radial distances. As an example, in Figure 7, we show the incident and transmitted continuum for HIGHION; clearly, there is no significant attenuation of the incident continuum, hence highly-ionized gas could exist in the “shadow” of a component similar to HIGHION, i.e., subtending the same solid angle with respect to the ionizing radiation. LOWION also produces weak attenuation. Assuming that density decreases with  $R$ , as observed with the optical emission-line gas (Kraemer & Crenshaw 2000a), each additional zone could be at roughly the same ionization state. There is some evidence for this scenario, in the sense that the optical continuum profile shows clear radial structure (Crenshaw & Kraemer 2000a). A series of separate shells would effectively create a large column density without violating the

$\Delta R/R$  constraint <sup>5</sup>, and thereby reduce the required covering factor.

This proposed structure of the NLR has implications for the origin of the polarized optical emission in NGC 1068, which is presumably due to scattering by free electrons. In their analysis of optical polarimetry of NGC 1068, Miller et al. (1991) determined that the temperature of the scattering medium is  $\sim 3 \times 10^5$  K; for comparison, the predicted temperature for HIGHION is  $5.15 \times 10^5$  K. However, the required column density of the medium is  $\gtrsim 10^{22}$  cm<sup>-2</sup> (Pier et al. 1994), or an order of magnitude greater than that of HIGHION. On the other hand, if the emission line region is comprised of a series of zones, described above, the total column density of high-ionization X-ray emission-line gas would be significantly larger than that of HIGHION. Therefore, we suggest that gas with physical conditions similar to those of HIGHION is the source of the scattered/polarized emission.

## 5. Conclusions

We analyzed an archival *XMM-Newton*/RGS spectrum of the Seyfert 2 galaxy NGC 1068, which was previously published by Kinkhabwala et al. (2002). In the process, we remeasured the emission-line fluxes, widths and radial velocities, and the fluxes and widths of RRCs, and, overall, obtained similar values to those of Kinkhabwala et al. (2002). We generated photoionization models, using Cloudy (Ferland et al. 2013), to fit the emission-line spectrum. Our main results are as follows.

1. Overall the X-ray emission-lines have radial velocities blue-shifted with respect to the systemic velocity of the host galaxy. The velocities and *FWHM* are roughly the same as that of [O III]  $\lambda 5007$ , which suggests that the X-ray gas is part of the mass outflow through the NLR. Although there is evidence for two kinematic components, with the N VI and O VII lines having more negative radial velocities than the N VII and O VIII lines, the differences are less than the measurement uncertainties.
2. Based on our preliminary modeling results, we determined the abundances of heavy elements in the emission-line gas to be overall  $1.5 \times$  solar. However, the carbon and nitrogen abundances are 3.2 and 6 times solar, respectively. One possibility is that an early period of star-formation produced much of the excess carbon, which was followed by conversion of carbon into nitrogen in a more recent period. Kallman et al. (2014) also suggested non-standard abundances for the emission-line gas, but did not discuss possible connections with

---

<sup>5</sup>Note that adding what are essentially identical ATABLES would not change the fit to the RGS spectra, hence it is impossible to test this scenario via XSPEC.

the star-formation history.

3. We were able to fit most of strong emission lines with two components, LOWION and HIGHION, characterized by  $\log U = -0.05$  and  $1.22$ , and  $\log N_{\text{H}} = 20.85$  and  $21.2$ , respectively. The LOWION produces most of the emission from He-like C, N, and O lines, while the HIGHION produces the H-like N, O, and Ne and most of the He-like Ne lines. The predicted electron temperature for LOWION is consistent with the measured widths of He-like RRCs, however that of HIGHION is several times higher than that derived from the H-like RRCs, which we attribute to uncertainties in the width measurements. Overall, the emission lines and RRCs are consistent with photoionization, albeit with a small contribution from photoexcitation for the resonance lines.

4. The covering factors determined for LOWION and HIGHION were  $0.35$  and  $0.84$ , which, while physically possible, are high given the likelihood that a fraction of the X-ray emission is undetected due to absorption by material in the disk of the host galaxy or surrounding the NLR. However, the transparency of these components to the ionizing radiation leads to the possibility that there are multiple zones of highly ionized gas which subtend the same solid angle. The additional emission from these zones would reduce the covering factors.

5. Our estimated total mass and mass outflow rates for LOWION and HIGHION are similar to the values determined by Kallman et al. (2014) from the *Chandra*/HETG spectra. Interestingly, the X-ray emission line gas likely represents the largest mass component of the NLR, which does not appear to be true of NGC 4151 (e.g. Armentrout et al. 2007).

6. The ionization state and temperature of HIGHION are consistent with those of the scattering medium in which the polarized emission arises (Miller et al. 1991; Kraemer & Crenshaw 2000a), although its column density is an order of magnitude too small. However, if there are multiple zones, as noted in item 4., the total column density of high-ionization gas could be sufficient to produce the scattered light. The radial profile of the continuum radiation (Crenshaw & Kraemer 2000a) is consistent with such a scenario. Therefore, we suggest that the scattered emission arises in the X-ray emission-line gas, in agreement with Ogle et al. (2003).

Finally, the overall properties of NGC 1068, including a high mass accretion rate, super-solar abundances, large amounts of highly ionized gas and molecular gas (e.g. Riffel et al. 2014), and active star-formation (Bruhweiler et al. 2001) may be connected to its stage of activity. That is, NGC 1068 is in an early part of its active phase, at which time the AGN is being rapidly fueled, but before the inner nucleus has been cleared.

## 6. Acknowledgments

This work was supported by NASA grant NNX10AD78G. This research has made use of the NASA/IPAC Extragalactic Database (NED), which is operated by the Jet Propulsion Laboratory, California Institute of Technology, under contract with the National Aeronautics and Space Administration. We thank the referee, Tim Kallman, for his careful review of the paper and constructive comments. We thank A. Maeder, M. Catalan, and E. Behar for useful suggestions. We also thank G. Ferland and associates for their continuing maintenance of Cloudy.

## REFERENCES

- Antonucci, R. R. J. 1993, *ARA&A*, 31, 473
- Armentrout, B., Kraemer, S., & Turner, T. 2007, *ApJ*, 665, 237
- Arnaud, K. A. 2010, in *Bulletin of the American Astronomical Society*, Vol. 42, AAS/High Energy Astrophysics Division #11, 668
- Asplund, M., Grevesse, N., & Sauval, A. J. 2005, in *Astronomical Society of the Pacific Conference Series*, Vol. 336, *Cosmic Abundances as Records of Stellar Evolution and Nucleosynthesis*, ed. T. G. Barnes, III & F. N. Bash, 25
- Awaki, H., Terashima, Y., Hayashida, K., & Sakano, M. 2001, *PASP*, 53, 647
- Bland-Hawthorn, J., Gallimore, J. F., Tacconi, L. J., et al. 1997, *Ap&SS*, 248, 9
- Blustin, A. J., Page, M. J., Fuerst, S. V., Branduardi-Raymont, G., & Ashton, C. E. 2005, *A&A*, 431, 111
- Bonatto, C. J., & Pastoriza, M. G. 1997, *ApJ*, 486, 132
- Bottorff, M. C., Korista, K. T., & Shlosman, I. 2000, *ApJ*, 537, 134
- Brinkman, A. C., Kaastra, J. S., van der Meer, R. L. J., et al. 2002, *A&A*, 396, 761
- Bruhweiler, F. C., Miskey, C. L., Smith, A. M., Landsman, W., & Malumuth, E. 2001, *ApJ*, 546, 866
- Capetti, A., Axon, D. J., & Macchetto, F. D. 1997, *ApJ*, 487, 560
- Carigi, L., Peimbert, M., Esteban, C., & Garca-Rojas, J. 2005, *ApJ*, 623, 213
- Crenshaw, D. M., & Kraemer, S. B. 2000a, *ApJ*, 532, 247

- . 2000b, *ApJ*, 532, L101
- . 2012, *ApJ*, 753, 75
- Crenshaw, D. M., Kraemer, S. B., & George, I. 2003, *ARA&A*, 41, 117
- Crenshaw, D. M., Kraemer, S. B., Schmitt, H. R., et al. 2010a, *AJ*, 139, 871
- Crenshaw, D. M., Schmitt, H. R., Kraemer, S. B., Mushotzky, R. F., & Dunn, J. P. 2010b, *ApJ*, 708, 419
- Das, V., Crenshaw, D. M., & Kraemer, S. B. 2007, *ApJ*, 656, 699
- Das, V., Crenshaw, D. M., Kraemer, S. B., & Deo, R. P. 2006, *AJ*, 132, 620
- Dickey, J. M., & Lockman, F. J. 1990, *ARA&A*, 28, 215
- Edelson, R. A., Alexander, T., Crenshaw, D. M., et al. 1996, *ApJ*, 470, 364
- Esteban, C., Garca-Rojas, J., Peimbert, M., et al. 2005, *ApJ*, 618, L95
- Evans, I. N., Ford, H. C., Kinney, A. L., et al. 1991, *ApJ*, 369, L27
- Everett, J. E., & Murray, N. 2007, *ApJ*, 656, 93
- Ferland, G. J., Korista, K. T., Verner, D. A., et al. 1998, *PASP*, 110, 761
- Ferland, G. J., Porter, R. L., van Hoof, P. A. M., et al. 2013, *Rev. Mexicana Astron. Astrofis.*, 49, 137
- Gallimore, J. F., Baum, S. A., O’Dea, C. P., Brinks, E., & Pedlar, A. 1994, *ApJ*, 422, L13
- George, I. M., Turner, T. J., Mushotzky, R., Nandra, K., & Netzer, H. 1998, *ApJS*, 114, 73
- Greenhill, L. J., & Gwinn, C. R. 1997, *Ap&SS*, 248, 261
- Grevesse, N., & Sauval, A. J. 1998, *Space Sci. Rev.*, 85, 161
- Halpern, J. 1984, *ApJ*, 281, 90
- Henry, R. B. C., Edmunds, M. G., & Kppen, J. 2000, *ApJ*, 541, 660
- Huchra, J. P., Vogeley, M. S., & Geller, M. J. 1999, *VizieR Online Data Catalog*, 212, 10287
- Kalberla, P. M. W., Burton, W. B., Hartmann, D., et al. 2005, *A&A*, 440, 775
- Kallman, T., Evans, D. A., Marshall, H., et al. 2014, *ApJ*, 780, 121
- Kallman, T. R., Palmeri, P., Bautista, M. A., Mendoza, C., & Krolik, J. H. 2004, *ApJS*, 155, 675

- Kinkhabwala, A., Sako, M., Behar, E., et al. 2002, *ApJ*, 575, 732
- Koski, A. T. 1978, *ApJ*, 223, 56
- Kraemer, S. B., & Crenshaw, D. M. 2000a, *ApJ*, 532, 256
- . 2000b, *ApJ*, 544, 763
- Kraemer, S. B., Ruiz, J. R., & Crenshaw, D. M. 1998, *ApJ*, 508, 232
- Kraemer, S. B., Schmitt, H. R., Crenshaw, D. M., et al. 2011, *ApJ*, 727, 130
- Kraemer, S. B., Trippe, M. L., Crenshaw, D. M., et al. 2009, *ApJ*, 698, 106
- Kriss, G. A., Davidsen, A. F., Blair, W. P., Ferguson, H. C., & Long, K. S. 1992, *ApJ*, 394, L37
- Krolik, J. H., & Kriss, G. A. 2001, *ApJ*, 561, 684
- Lutz, D., Sturm, E., Genzel, R., et al. 2000, *ApJ*, 536, 697
- Maeder, A., & Meynet, G. 1989, *A&A*, 210, 155
- Meléndez, M., Kraemer, S. B. and Armentrout, B. K., Deo, R. P., et al. 2008, *ApJ*, 682, 94
- Miller, J. S., Goodrich, R., & Mathews, W. G. 1991, *ApJ*, 378, 47
- Netzer, H. 1993, *ApJ*, 411, 594
- . 1996, *ApJ*, 473, 781
- Ogle, P. M., Brookings, T., Canizares, C. R., Lee, J. C., & Marshall, H. L. 2003, *A&A*, 402, 849
- Ogle, P. M., Marshall, H. L., Lee, J. C., & Canizares, C. R. 2000, *ApJ*, 545, L81
- Peimbert, M. 1967, *ApJ*, 150, 825
- Peterson, B. M., Ferrarese, L., Gilbert, K. M., et al. 2004, *ApJ*, 613, 682
- Pier, E. A., Antonucci, R., Hurt, T., Kriss, G., & Krolik, J. 1994, *ApJ*, 428, 124
- Pogge, R. W. 1988, *ApJ*, 328, 519
- Porquet, D., & Dubau, J. 2002, in *SF2A-2002: Semaine de l’Astrophysique Francaise*, ed. F. Combes & D. Barret, 371
- Porter, R. L., Ferland, G. J., Kraemer, S. B., et al. 2006, *PASP*, 118, 920
- Riffel, R. A., Vale, T. B., Storchi-Bergmann, T., & McGregor, P. J. 2014, *MNRAS*, 442, 656

Seaton, M. J. 1978, MNRAS, 185, 5P

—. 1979, MNRAS, 187, 73P

Sofue, Y. 1991, PASJ, 43, 671

Tully, R., Rizzi, L., Shaya, E., et al. 2009, AJ, 138, 323

Turner, T. J., Kraemer, S. B., Mushotzky, R. F., George, I. M., & Gabel, J. R. 2003, ApJ, 594, 128

Whittle, M. 1992, ApJS, 79, 49

Wilms, J., Allen, A., & McCray, R. 2000, ApJ, 542, 914

Young, A. J., Wilson, A. S., & Shopbell, P. L. 2001, ApJ, 556, 6



Table 1: Comparison of the Observed and Predicted Emission-Line Fluxes

Line ID	Observed <sup>a</sup>	Absorption-corrected	Total Model <sup>b</sup>	Low U <sup>c</sup>	High U <sup>d</sup>
C v He $\beta$	1.16 $\pm$ 0.31	3.24 $\pm$ 0.86	1.09	1.09	
C v He $\delta$	2.45 $\pm$ 1.30	4.62 $\pm$ 2.08	0.59	0.59	
C vi Ly $\alpha$	9.48 $\pm$ 0.41	23.35 $\pm$ 1.01	16.57	9.55	7.02
C vi Ly $\beta$	1.76 $\pm$ 0.21	3.18 $\pm$ 0.38	2.58	0.87	1.71
C vi Ly $\gamma$	0.60 $\pm$ 0.14	0.95 $\pm$ 0.22	1.41	0.53	0.88
C vi Ly $\delta$	1.07 $\pm$ 0.16	1.94 $\pm$ 0.29	0.87	0.41	0.46
N vi He $\gamma$	0.47 $\pm$ 0.14	0.67 $\pm$ 0.20	0.42	0.42	
N vi $r$	3.32 $\pm$ 0.48	6.08 $\pm$ 0.87	4.13	3.62	0.51
N vi $i$	0.93 $\pm$ 0.37	1.72 $\pm$ 0.68	1.80	1.80	
N vi $f$	7.37 $\pm$ 0.12	13.20 $\pm$ 0.60	9.77	9.77	
N vii Ly $\alpha$	6.01 $\pm$ 0.26	8.92 $\pm$ 0.39	6.45	1.99	4.46
N vii Ly $\beta$	0.95 $\pm$ 0.09	1.45 $\pm$ 0.16	1.62	0.43	1.19
N vii Ly $\gamma$	0.40 $\pm$ 0.16	0.53 $\pm$ 0.16	0.88	0.27	0.61
N vii Ly $\delta$	0.35 $\pm$ 0.10	0.40 $\pm$ 0.10	0.51	0.19	0.32
O vii $r$	4.96 $\pm$ 0.28	7.85 $\pm$ 0.68	5.30	3.97	1.33
O vii $i$	1.00 $\pm$ 0.44	1.94 $\pm$ 0.70	3.13	3.13	
O vii $f$	9.25 $\pm$ 0.18	14.99 $\pm$ 0.29	12.57	12.07	0.50
O vii He $\beta$	0.73 $\pm$ 0.15	0.99 $\pm$ 0.22	0.88	0.54	0.34
O vii He $\gamma$	0.67 $\pm$ 0.09	0.88 $\pm$ 0.14	0.36	0.36	
O vii He $\delta$	0.38 $\pm$ 0.08	0.49 $\pm$ 0.12	0.30	0.30	
O viii Ly $\alpha$	5.37 $\pm$ 0.30	7.44 $\pm$ 0.64	8.94	1.25	7.69
O viii Ly $\beta$	0.96 $\pm$ 0.44	1.22 $\pm$ 0.28	1.59	0.32	1.27
Ne ix $r$	1.74 $\pm$ 0.13	2.08 $\pm$ 0.15	1.46	0.45	1.01
Ne ix $f$	1.11 $\pm$ 0.15	1.32 $\pm$ 0.18	0.79	0.38	0.41
Ne ix He $\beta$	0.21 $\pm$ 0.09	0.24 $\pm$ 0.09	0.45	0.16	0.29
Ne x Ly $\alpha$	1.34 $\pm$ 0.11	1.52 $\pm$ 0.12	2.07		2.07
Mg xi $rif$	0.90 $\pm$ 0.17	0.96 $\pm$ 0.19	1.46		1.46
Mg xii Ly $\alpha$	0.27 $\pm$ 0.11	0.29 $\pm$ 0.12	0.95		0.95

<sup>a</sup> Fluxes obtained by fitting Gaussian to each line as identified in the combined spectra of RGS 1 & 2.; all fluxes  $\times 10^{-4}$  photons cm $^{-2}$  s $^{-1}$ .

<sup>a</sup> Absorption-corrected line fluxes predicted by CLOUDY in the total model.

<sup>b</sup> Fluxes predicted by CLOUDY for LOWION, after scaling to that of O vii  $f$ .

<sup>c</sup> Fluxes predicted by CLOUDY for HIGHION, after scaling to that of O viii Ly $\alpha$ .

Table 2: Observed Energies and Velocity Shifts Relative to Systemic

Line ID	$\lambda_{\text{th}}^{\text{a}}$ (Å)	$E_{\text{th}}^{\text{b}}$ (eV)	$\Delta E^{\text{c}}$ (eV)	Velocity shift <sup>d</sup> (km s <sup>-1</sup> )
C v He $\beta$	34.9728	354.516	$0.444 \pm 0.085$	$-490 \pm 80$
C v He $\delta$	32.7542	378.529	$0.969 \pm 0.205$	$-680 \pm 120$
C vi Ly $\alpha$	33.7342	367.533	$0.333 \pm 0.019$	$-270 \pm 50$
C vi Ly $\beta$	28.4663	435.547	$0.582 \pm 0.065$	$-400 \pm 70$
C vi Ly $\gamma$	26.9900	459.369	$0.618 \pm 0.040$	$-400 \pm 80$
C vi Ly $\delta$	26.3572	470.399	$0.459 \pm 0.135$	$-290 \pm 10$
N vi He $\gamma$	23.7710	521.578	$0.685 \pm 0.161$	$-400 \pm 110$
N vi r	28.7870	430.695	$0.376 \pm 0.042$	$-260 \pm 60$
N vi i	29.0815	426.333	$0.342 \pm 0.069$	$-240 \pm 70$
N vi f	29.5343	419.797	$0.495 \pm 0.018$	$-350 \pm 60$
N vii Ly $\alpha$	24.7792	500.356	$0.318 \pm 0.045$	$-190 \pm 70$
N vii Ly $\beta$	20.9095	592.957	$0.498 \pm 0.141$	$-251 \pm 102$
N vii Ly $\gamma$	19.8261	625.358	$0.513 \pm 0.161$	$-250 \pm 110$
N vii Ly $\delta$	19.3614	640.368	$0.841 \pm 0.235$	$-390 \pm 130$
O vii r	21.6020	573.947	$0.483 \pm 0.046$	$-250 \pm 80$
O vii i	21.8044	568.620	$0.539 \pm 0.111$	$-280 \pm 90$
O vii f	22.1012	560.983	$0.708 \pm 0.029$	$-380 \pm 70$
O vii He $\beta$	18.6270	665.615	$1.516 \pm 0.174$	$-680 \pm 120$
O vii He $\gamma$	17.7682	697.787	$1.414 \pm 0.221$	$-610 \pm 130$
O vii He $\delta$	17.3958	712.722	$1.145 \pm 0.310$	$-480 \pm 150$
O viii Ly $\alpha$	18.9725	653.493	$0.337 \pm 0.036$	$-150 \pm 80$
O viii Ly $\beta$	16.0067	774.577	$-0.111 \pm 0.194$	$+40 \pm 120$

<sup>a</sup> Theoretical wavelengths from NIST/Kentucky atomic database.

<sup>b</sup> Theoretical line energies.

<sup>c</sup>  $\Delta E = E_{\text{obs}} - E_{\text{th}}$ , with uncertainties of  $1\sigma$  (68% confidence level).

<sup>d</sup> The quoted errors are statistical ( $1\sigma$ ) and systematic (derived from the centroid position uncertainty), combined in quadrature.

Table 3. Photoionization Model Parameters<sup>a</sup>

Component	logU	logN <sub>H</sub> <sup>b</sup>	velocity <sup>c</sup>
LOWION	$-0.05^{+0.02}_{-0.02}$	$20.85^{+0.03}_{-0.05}$	$215^{+12}_{-22}$
HIGHION	$1.23^{+0.01}_{-0.01}$	$21.2^{+0.00}_{-0.001}{}^d$	$166^{+23}_{-39}$

<sup>a</sup>Fit statistics:  $\chi^2 = 9805.83$  using 4926 PHA bins. Reduced  $\chi^2 = 1.99508$  for 4915 degrees of freedom.

<sup>b</sup>N<sub>H</sub> in units of cm<sup>-2</sup>

<sup>c</sup>Velocity offset (km s<sup>-1</sup>) from systemic.

<sup>d</sup>Upper limit fixed based on  $\Delta R/R$  constraint (see Section 3.2.1).

Table 4. Measured and Model-Predicted RRC Parameters

Ion	kT (eV)	Flux <sup>a</sup>	Model Total	LOWION	HIGHION
C v	2.39±0.50	11.25±0.90	6.51	6.51	
C vi	8.13±2.10	9.25±0.91	9.62	2.48	4.03
N vi	1.01±0.33	1.40±0.13	2.56	2.56	
N vii	6.56±0.30	4.38±0.16	3.03	0.77	2.26
O vii	4.50±0.25	2.97±0.30	4.46	4.15	0.31

<sup>a</sup>All fluxes  $\times 10^{-4}$  photons cm<sup>-2</sup> s<sup>-1</sup>

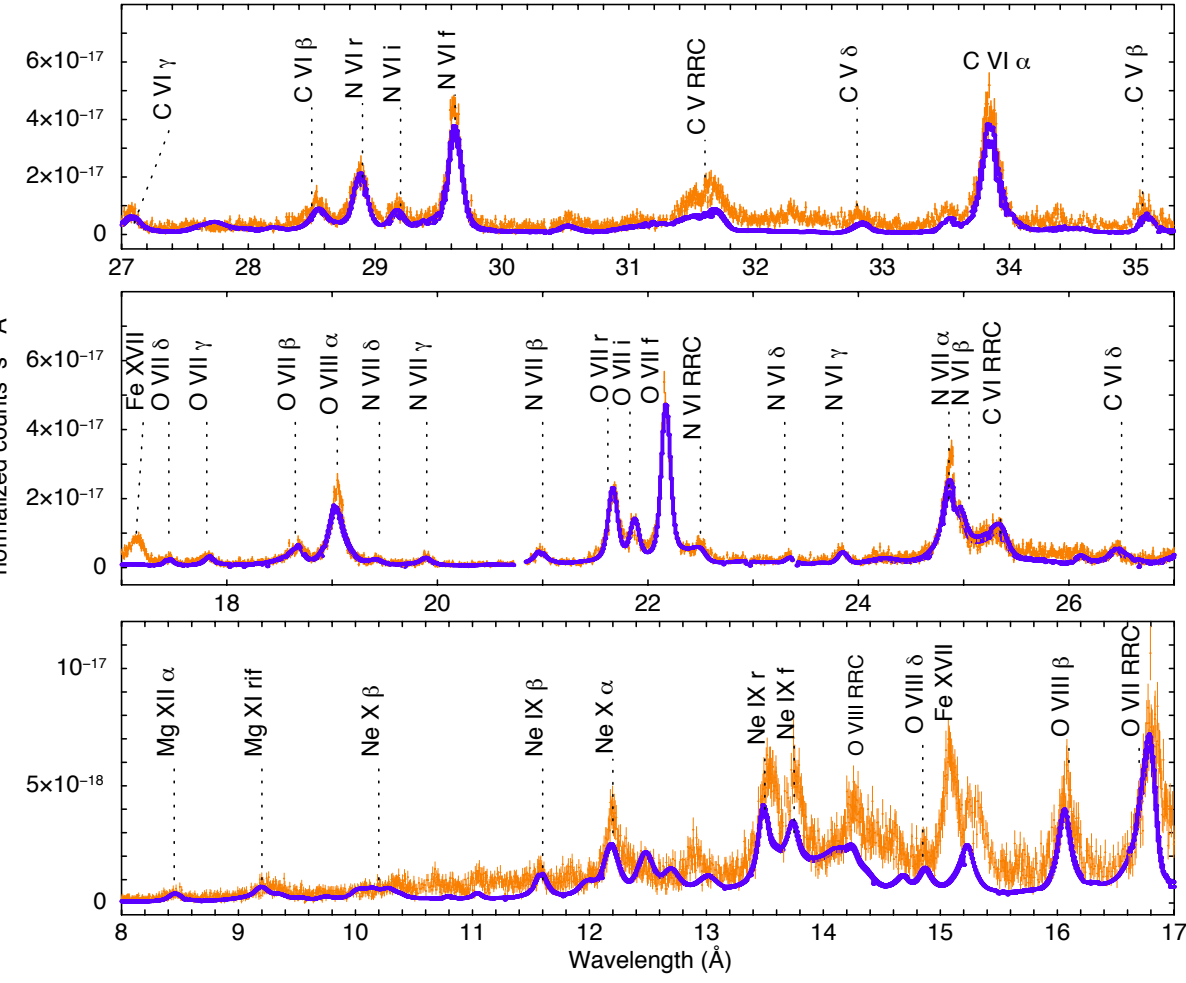


Fig. 1.— The total model comprising of both the zones (blue) compared to the combined RGS1 and RGS2 spectrum (orange). Note that the model produces a fairly good fit, except for  $\lambda < 17\text{\AA}$ , as discussed in Section 3.2.1.

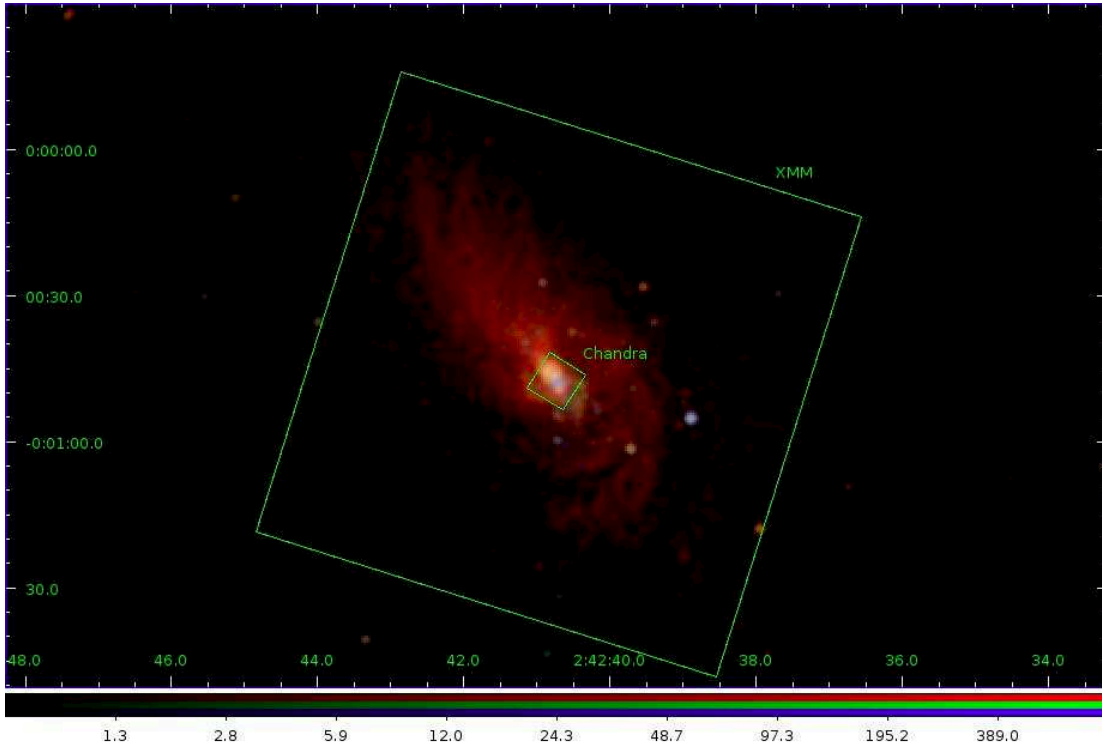


Fig. 2.— XMM/RGS and *Chandra* extraction cells, overlaid on the *Chandra*/ACIS image. Declination is along the y-axis and Right Ascension is along the x-axis and the colors in the image correspond to the following: red, 0.2 - 1.5 keV; green, 1.5 - 2.5 keV; and blue, 2.5 - 8.0 keV. The extraction cells are square with size of  $\sim 100''$  and  $\sim 9''$  for XMM/RGS and *Chandra*/HETG, respectively, oriented with respect to the roll angles for these observations (Kinkhabwala et al. 2002; Kallman et al. 2014).

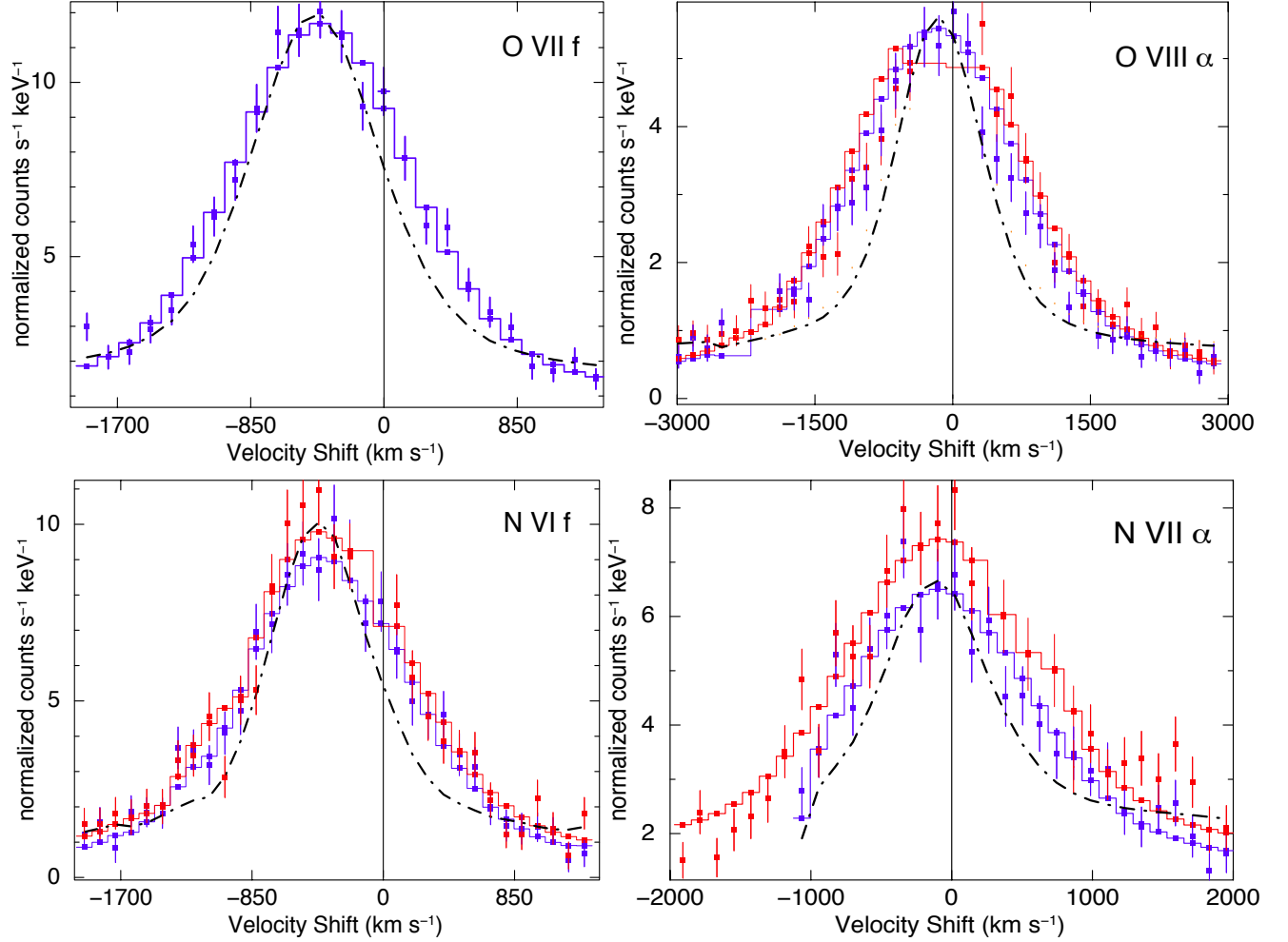


Fig. 3.— RGS 1 (*red*) and RGS 2 (*blue*) line profiles for O VII  $f$ , O VIII Ly $\alpha$ , N VI  $f$  and N VII, relative to the nucleus. The systemic velocity of the host galaxy is represented here by the solid line at 0 km s<sup>-1</sup>. Note the blueshifts of each emission-line peak. Each line is broadened than the instrument profile which is represented by the dotted line.

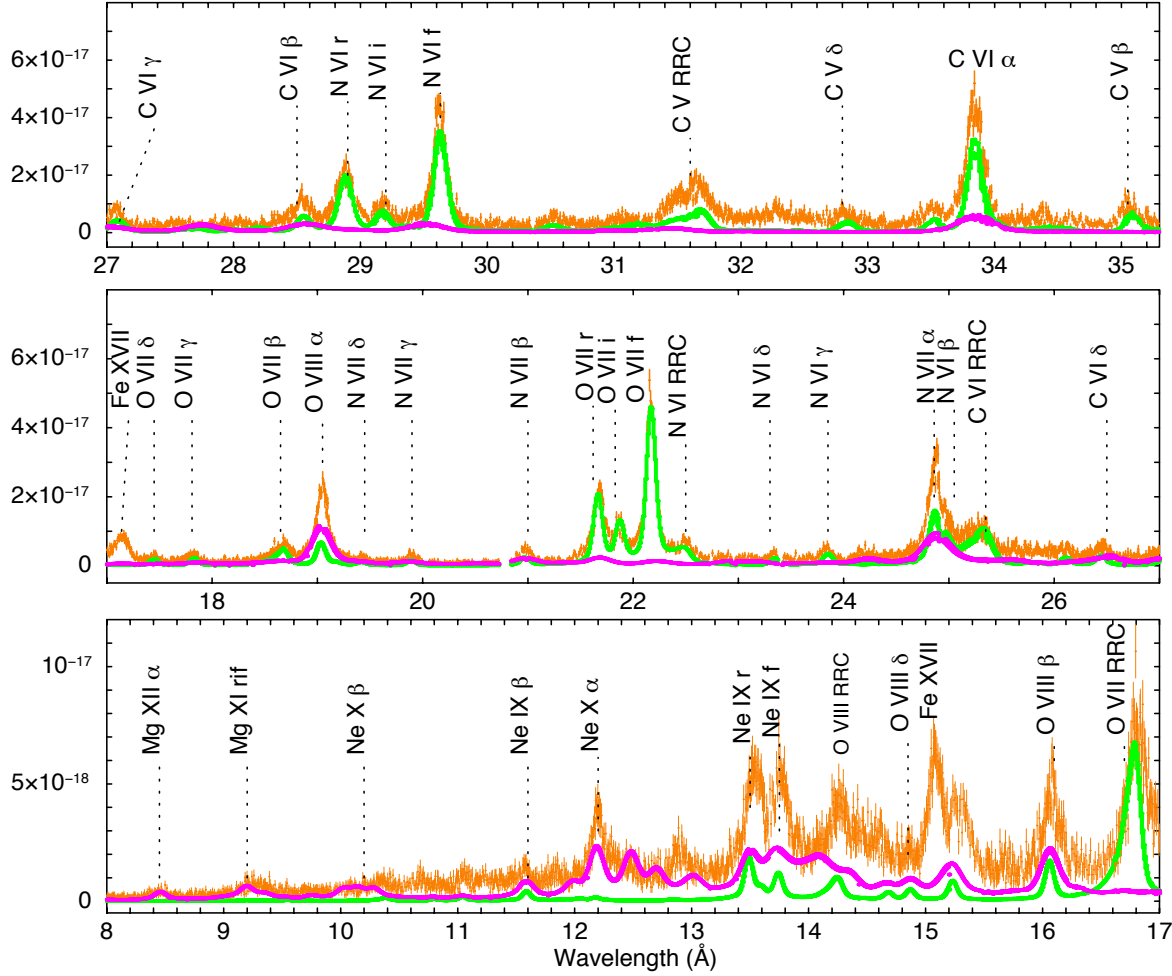


Fig. 4.— The individual model components, LOWION (green) and HIGHION (purple) compared to the combined RGS1 and RGS2 spectrum. As noted in the text, LOWION contributes most of the emission from the He-like C, N, and O, while HIGHION contributes most of the H-like N and O and both H and He-like Ne emission.



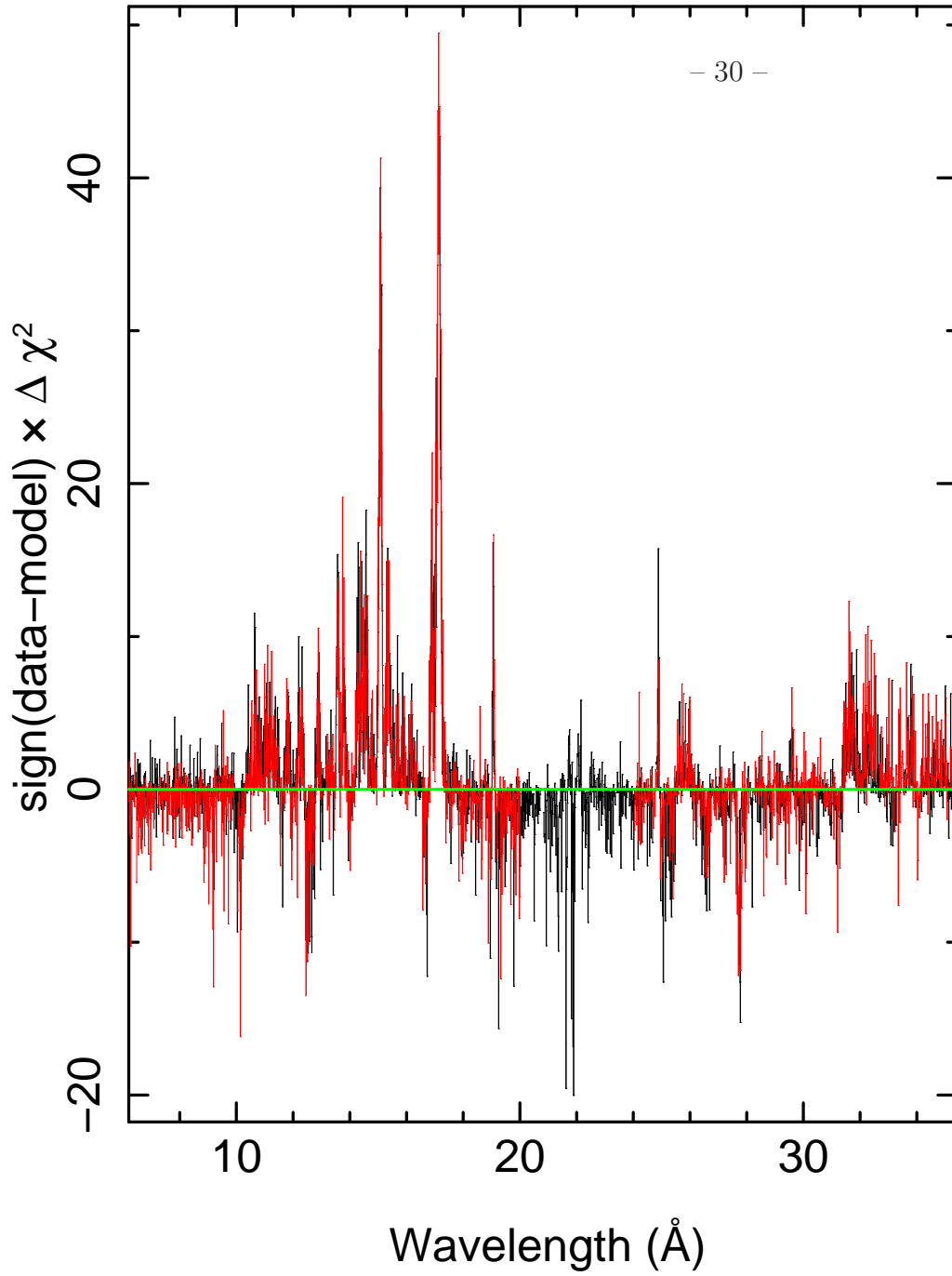


Fig. 5.— The contributions to  $\chi^2$  for the data compared to the best fitting two-zone model from XSPEC, detailed in Section 3. RGS 1 data are shown in black, RGS 2 data are shown in red. The gaps are where the dispersed RGS spectrum falls upon a non-operational CCD chip. The greatest mis-match occurs in the range of 14Å–17Å and is primarily due to the under-prediction of emission lines from M-shell Fe ions.

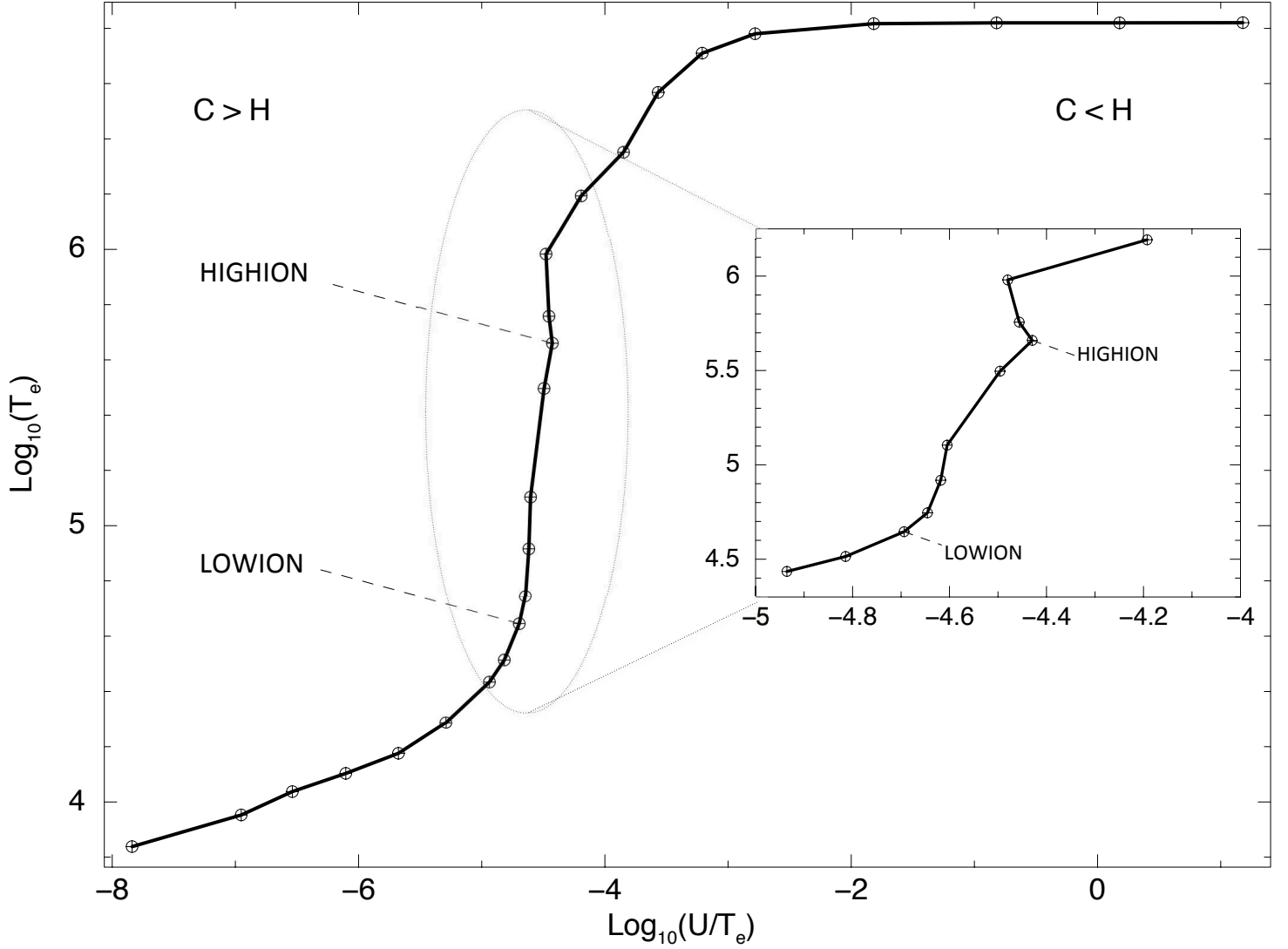


Fig. 6.— Stability curve for a range of ionization parameter from  $10^{-3}$  to  $10^7$  and our assumed SED and abundances (see Section 3.1). The regions at the left and right of the curve are where the cooling and heating dominate, respectively, as indicated. The two gas components identified from our photoionization modeling, LOWION and HIGHION, lie on stable, i.e., positively-sloped portions of the curve (which is most clearly seen via the insert), although the latter is close to an unstable region.

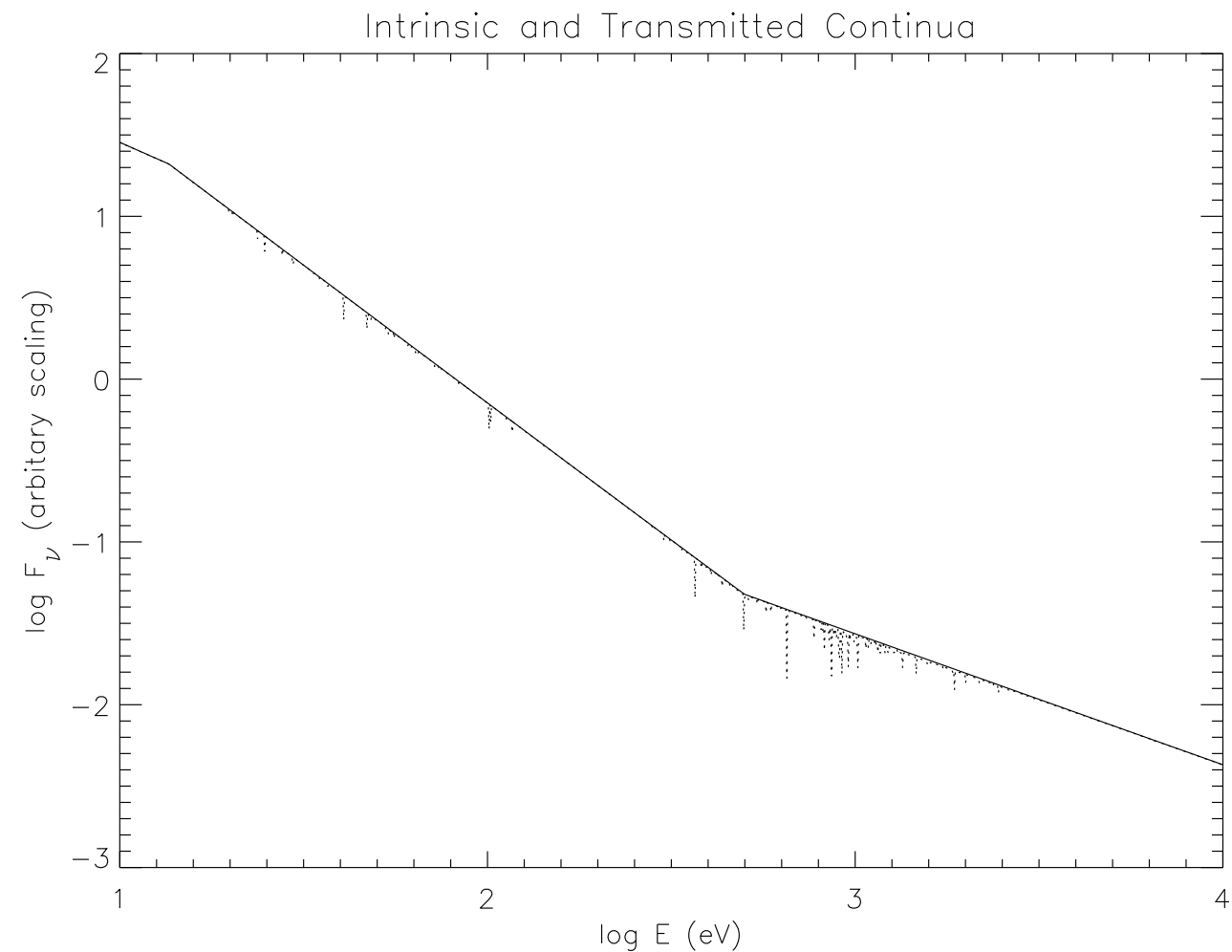


Fig. 7.— Incident (solid-line) and Transmitted (dotted-line) model continua for the component HIGHION. As shown, there is little attenuation of the ionizing radiation as it is transmitted, hence gas can be in a similar state of ionization in the “shadow” of the component.